ACS APPLIED MATERIALS & INTERFACES

Subscriber access provided by CORNELL UNIVERSITY LIBRARY

Article

Nanoarchitectonics of Small Molecule and DNA for Ultrasensitive Detection of Mercury

Pandeeswar Makam, Satyaprasad P Senanayak, and Thimmaiah Govindaraju

ACS Appl. Mater. Interfaces, **Just Accepted Manuscript** • DOI: 10.1021/acsami.6b10527 • Publication Date (Web): 18 Oct 2016

Downloaded from http://pubs.acs.org on October 18, 2016

Just Accepted

"Just Accepted" manuscripts have been peer-reviewed and accepted for publication. They are posted online prior to technical editing, formatting for publication and author proofing. The American Chemical Society provides "Just Accepted" as a free service to the research community to expedite the dissemination of scientific material as soon as possible after acceptance. "Just Accepted" manuscripts appear in full in PDF format accompanied by an HTML abstract. "Just Accepted" manuscripts have been fully peer reviewed, but should not be considered the official version of record. They are accessible to all readers and citable by the Digital Object Identifier (DOI®). "Just Accepted" is an optional service offered to authors. Therefore, the "Just Accepted" Web site may not include all articles that will be published in the journal. After a manuscript is technically edited and formatted, it will be removed from the "Just Accepted" Web site and published as an ASAP article. Note that technical editing may introduce minor changes to the manuscript text and/or graphics which could affect content, and all legal disclaimers and ethical guidelines that apply to the journal pertain. ACS cannot be held responsible for errors or consequences arising from the use of information contained in these "Just Accepted" manuscripts.

ACS Publications

ACS Applied Materials & Interfaces is published by the American Chemical Society.
1155 Sixteenth Street N.W., Washington, DC 20036
Published by American Chemical Society. Copyright © American Chemical Society.
However, no copyright claim is made to original U.S. Government works, or works produced by employees of any Commonwealth realm Crown government in the course of their duties.

Nanoarchitectonics of Small Molecule and DNA for Ultrasensitive Detection of Mercury

M. Pandeeswar,[†] *Satyaprasad P. Senanayak,*[‡] *and T. Govindaraju**[,†]

[†]Bioorganic Chemistry Laboratory, New Chemistry Unit, Jawaharlal Nehru Centre for Advanced Scientific Research, Jakkur P.O., Bengaluru 560064, Karnataka, India.

[‡]Molecular Electronics Lab, Chemistry and Physics of Materials Unit, Jawaharlal Nehru Center for Advanced Scientific Research, Jakkur P.O., Bengaluru, 560064, Karnataka, India.

KEYWORDS: environmental pollutant, ultra sensitive detection of mercury, small organic semiconductor-DNA nanoarchitectonics, chiroptical and electrical detection

ABSTRACT

Reliable and ultrasensitive detection of mercury ions is of paramount importance for toxicology assessment, environmental protection and human health. Herein, we present a novel optoelectronic approach based on nanoachitectonics of small molecule templated DNA system that consists of an adenine (A) conjugated small organic semiconductor (BNA) and deoxyribo-oligothymidine (dT_n). This mutually templated dynamic chiral co-assembly system (BNAn-dT_n) with tunable chiroptical, morphological and electrical properties is tapped in to enable ultra-sensitive and selective detection of inorganic and organometallic mercury in water. We observe a rapid transformation of the BNA_n-dT_n co-assembly into a metallo-DNA duplex $[dT\text{-}Hg\text{-}dT]_n$ in the presence of mercury which is utilized for a chiro-optical and conductivity based rapid and sub-nanomolar sensitivity (≥ 0.1 nM, 0.02 ppb) to mercury ions in water (~ 100 times lower than United States Environmental Protection Agency tolerance limit). This ultra-sensitive detection of inorganic and organometallic mercury is driven by a novel chemical design principle which allows strong mercury thymine interaction. This study is anticipated to inspire the development of future templated DNA nanotechnology based optoelectronic devices for the rapid and ultrasensitive detection of numerous other toxic analytes.

1. INTRODUCTION

Monitoring ultra-low concentration levels of toxic heavy metal ions in the ecosystem is crucial owing to their widespread adverse impacts on human health and the environment.[1-3] Mercury (Hg) is one of the most predominant heavy metals in the environment with both natural (volcanic and oceanic emissions) and anthropogenic (major industrial sources, such as coal and gold mining, and fossil fuel combustion) sources and exists in multiple forms (i.e., elemental (Hg^0), inorganic salts (Hg^{2+}) and organometallic compounds (CH_3Hg^+ and CH_3HgCH_3)).[4] Alarmingly, very low concentrations of mercury in any form (neutral or ionic) can be readily absorbed by the human body and accumulate in the brain, heart, kidneys and lungs owing to tight binding to proteins, which can cause fatal diseases.[5-6] Contaminated natural bodies of water, drinking water and parts of the food chain, particularly fish, are considered some of the major sources of mercury exposure for humans.[7] Despite its high toxicity, mercury has been widely used for decades as a chemical additive and energy source in many industrial applications, including cosmetics, thermometers, batteries, agricultural chemicals and fluorescent lamps. Owing to the increasing threat and adverse effects of mercury on human health and the environment, the use and manufacture of mercury-based products have been regulated by many developed countries. According to a United States Environmental Protection Agency (USEPA) report, the maximum permissible level of Hg^{2+} in food and drinking water is ~2 ppb (~10 nM).[5] Therefore, selective and sensitive detection of different forms of mercury at ultra-low concentrations is important for eliminating potential hazards as well as protecting and maintaining good human health. Many efforts have been focused on developing methods for the detection of mercury using various spectroscopic,[8-29] electrochemical[30-31] and conductivity[32-35] based techniques. However, low selectivity and sensitivity or the ecological footprint of the sensor materials used in these

techniques limit their application. Hence, development of a selective and ultrasensitive detection method to monitor different forms of mercury in situations that involve matters of public health is of paramount importance.

Strong and specific thymine-mercury-thymine (T-Hg-T) interactions[36-39] have been used as a promising approach for the selective detection of Hg^{2+}.[8,14,16,18,21-22,40-46] Several colorimetric and fluorometric sensors that are based on thymine and contain DNA sequence-functionalised gold nanoparticles,[18,40-43] fluorophores,[8,44] hydrogels[16,45] and DNA-based machines[8,14,21,46] have been developed. The templated DNA nanotechnology approach[47-49] was selected for the development of a sensor platform for mercury with high selectivity and sensitivity, robustness or stability, rapid detection time and low cost. Herein, we report a novel nanoarchitectonics[50-55] of mutually templated organic semiconductor (adenine conjugated naphthalenediimide, BNA) and complementary (thymine) single strand (ss) DNA (deoxyribo-oligothymidine: dT_n) for the ultrasensitive detection of mercury based on the changes in the chiroptical signal and electrical conductivity. Surprisingly, dT_ns with n>6 have not been employed to achieve an extended metallo-DNA duplex ($[dT\text{-}Hg\text{-}dT]_n$), probably because of the lack of an appropriate molecular design to drive the formation of these extended structures. In principle, a successful molecular design involving relatively longer dT_n sequences would significantly enhance the sensitivity of detection compared to those in previous studies where mixed aptamers and ssDNA containing only a few thymine units have been used. We choose to use longer homothymidine sequences (dT_n, n= 6, 10, 20) in the form of a mutually templated and noncovalent co-assembly with BNA and its transformation into metallo-DNA as the platform for the detection of ultra-low concentrations of mercury. In our design, the molecular template (BNA) strategically contains a butyl group to support noncovalent hydrophobic interactions and an NDI-core for aromatic π–π

interaction and to serve as an electrically active moiety for electrical conductivity-based measurements.[54,56-58] Adenine (A) was selected as a complementary nucleobase to facilitate interactions with thymine units of dT_n through Watson-Crick (WC) hydrogen bonding, which is supported by the hydrophobic (butyl) and aromatic π–π (NDI core) interactions, to aid the mutually templated and extended co-assembly of BNA and dT_n. Although DNA templated dyes, extended π–conjugated systems and polymers have been previously studied, the conductivity property and sensor applications of these systems have not been investigated.[47-49,59-69] Herein, we exploit the intrinsic property of dT_n for complementary base pairing with stacks of adenine containing BNA to achieve a mutually templated and chiral co-assembly with functional properties suitable for the ultrasensitive detection of mercury (Figure. 1). Interestingly, the BNA alone self-assembles into 1D tapes. However, the mutually templated co-assembly of BNA_n-dT_n forms 2D sheets with variable lateral dimensions that depend on the dT_n sequence length, which demonstrates the tunability of the 2D nanostructures (Figure. 1). This templated co-assembly behaviour allowed us to modulate the chiroptical, morphological and conductivity properties of BNA_n-dT_n. Furthermore, the BNA_n-dT_n co-assembly enabled us to achieve maximum thymine-mercury interactions in the form of a mercury supported metallo-DNA duplex ($[dT\text{-}Hg\text{-}dT]_n$). The transformation of BNA_n-dT_n into a $[dT\text{-}Hg\text{-}dT]_n$ metallo-DNA duplex gives rise to distinct chiroptical, morphological and electrical conductivity properties that can be exploited for use as a highly selective and sensitive opto-electronic sensor for mercury detection in solution and a thin film state (Figure. 1). Remarkably, the BNA_n-dT_n sensor platform enabled the rapid detection of organic (CH_3Hg) and inorganic (Hg^{2+}) mercury in water with sensitivity to ultra-low concentrations of ≥ 0.1 nM (0.02 ppb), which is 100-fold lower than the USEPA tolerance limit (10 nM, 2 ppb).

2. RUSUTS AND DISCUSSION

2.1. Design and synthesis of BNA

N-butyl and adenine-functionalised naphthalenediimide (BNA) was synthesised via a two-step reaction route. 1,4,5,8-Naphthalenetetracarboxylic dianhydride (NDA) was substituted with n-butylamine and 9-(2-aminoethyl)-9H-purin-6-amine as the imide functionalities to obtain asymmetrically functionalised BNA in good yield. In the BNA molecular template, the adenine on one end is expected to hydrogen bond with the complementary thymines of dT_n through WC base pairing, and the n-butyl chain on the other end is expected to provide hydrophobic van der Waal interactions to support extended NDI-NDI π–stacking to form a helical co-assembly (i.e., BNA_n-dT_n) (Figure. 1).[70]

2.2. Nanoarchitectonics of small molecule templated dT_n co-assembly

The mutually templated co-assembly of BNA (100 μM) and dT_{10} was investigated by photophysical measurements upon mixing in phosphate-buffered saline (PBS, 10 mM, pH = 7, 5% DMSO) at 294 K. The UV-Vis absorption spectra of BNA contained broad absorption bands at 300-420 nm (band-I) and 220-260 nm (band-II), which correspond to π–π* transitions polarised along the long and short axis of the stacked NDI chromophores, respectively. In addition, dT_{10} exhibited an intense broad absorption band at 263 nm. Interestingly, upon mixing BNA with dT_{10} in a 1:1 ratio (BNA:T of dT_{10}), a significant hypochromic effect followed by a bathochromic shift in the band-I absorption maxima were observed, suggesting edge-to-face (J-type) π–stacked NDI chromophores with dT_{10} wrapped around the stack. To understand the long-range molecular orientations within the co-assembly of BNA and dT_{10}, we carried out circular dichroism (CD) spectroscopic studies owing to its ability to provide rapid assessment of induced chiral organisation in the mutually templated co-assembly (Figure. 2). BNA (100 μM)

independently exhibited a flat CD signal in the 250-420 nm absorption region, indicating the absence of any preferential helical order in its organisation. The complementary dT_{10} (10 μM) alone exhibited a bisignate CD cotton effect with a negative maximum at 250 nm and a positive maximum at 276 nm. Remarkably, upon mixing dT_{10} with BNA, the CD spectrum exhibited intense negative induced CD (ICD) signals in the band-II (220-260 nm) and band-I (300-420 nm) absorption regions of the NDI chromophore. The observed ICD signal with a negative maximum at 400 nm corresponded to π–stacked NDI chromophores (Figure. 2a), which revealed the left-handed (*M*-type) helical organisation of BNA accompanied by edge-to-face stacking of transition dipoles along the NDI long axis upon co-assembly with dT_{10} (Figure. 2a).[71-72] At this stage, although we assume that dT_{10} in BNA_{10}-T_{10} has a left-handed helical organization owing to the mutually templated co-assembly, the overlap of the NDI band II (240- 260 nm) absorption region with that of the nucleobase absorption complicated the assignment. However, our subsequent studies, which are discussed in the following sections, confirmed that dT_{10} adopted a left-handed structure in the mutually templated hybrid co-assembly. Furthermore, the attenuated total reflection infrared (ATR-IR) spectrum of BNA exhibited a N-H (adenine-NH_2) symmetric stretching frequency at 3419 cm^{-1}, and upon mixing with dT_{10}, this band shifted to a lower wavenumber (3366 cm^{-1}, broad) (Figure. S3).[70] The significant change ($\Delta\nu \sim 53$ cm^{-1}) in the N-H symmetric stretching frequency indicated hydrogen bonding interactions among the complementary base pairs (i.e., adenines bases of BNA molecules interact with thymines of dT_{10} through form WC base pairing, Figure. S3), which is one of the main driving forces for the formation of the mutually templated helical co- assembly of BNA_{10}-dT_{10}.

The nucleobase preference and selectivity for the mutually templated chiral co-assembly of BNA with deoxyribo-oligonucleotides (dB_{10}, B = A/T/G/C) were assessed by evaluating the

interaction of BNA with four different dB_{10} ($dA_{10}/T_{10}/G_{10}/C_{10}$) (Figure. 2b). The CD data revealed that among all of the dB_{10}, only complementary dT_{10} exhibited an ICD in the 300-420 nm region, which confirms that WC base pairing (A=T) is one of the main driving forces for the formation of the BNA_{10}-dT_{10} helical co-assembly. To determine the binding stoichiometry, CD Job-titration experiments were performed by keeping the total number of binding sites constant but varying the dT_{10} and BNA concentration ratio ([BNA]+[dT_{10}]= 110 μM with fraction of BNA in BNA_{10}-dT_{10} (f) = [BNA]/110 μM). The Job plot generated by monitoring the CD ellipticity (θ) at 400 nm as a function of f contained an inflection point at f= 0.5, and this point corresponds to a thymine (in dT_{10}): BNA ratio of 1:1. Therefore, the Job plot data revealed that the number of BNA molecules that bind to dT_{10} is equal to the number of thymine units in dT_{10} to form the mutually templated BNA_{10}-dT_{10} co-assembly (Figure. 2c). Systems driven by hydrogen bonding strongly depend on the pH of the media, and therefore, the impact of pH on the BNA_{10}-dT_{10} co-assembly at 293 K was investigated (Figure. 2d). The pH of the BNA_{10}-dT_{10} solution was varied from strongly basic to acidic (pH = 11 to 1), and the ICD signal at 400 nm was monitored. The maximum ICD intensity was observed under neutral conditions (pH = 8-6). However, basic (pH= 11-8) and acidic (pH= 2-6) conditions resulted in a decrease in the ICD intensity. Interestingly, under strongly acidic conditions (pH = 1), a relatively less intense but inverted (negative to positive) ICD signal was observed. This chiroptical switching is most likely due to protonation of the adenine moiety of BNA, which triggers chiral inversion through additional electrostatic interactions between negatively charged phosphate groups on the dT_{10} backbone and positively charged adenine (AH^+) of BNA.[73] Next, we studied the influence of the dT_n sequence length on the BNA_n-dT_n co-assembly by varying the sequence length of dT_n (n= 6, 10 and 20) and employing various spectroscopic techniques (Figure. 2e). Upon mixing of BNA

(100 μM) with dT_n (n= 6, 10 and 20) in a stoichiometric ratio of 1:1 (BNA:T), the CD spectra exhibited an ICD signal at 400 nm with a gradual increase in the CD ellipticity (θ) values as a function of the dT_n sequence length [-67.5° (BNA_6-dT_6), -83.3° (BNA_{10}-dT_{10}) and -92.2° (BNA_{20}-dT_{20})] (Figure. 2d). Similarly, the extent of bathochromic shift of the band-I absorption maxima in the UV-Vis absorption spectra varied with dT_n the sequence length ($\Delta\lambda_{max}$ ~ 3.0, 6.5, 9.5 nm for dT_6, dT_{10}, dT_{20}, respectively), indicating control over the degree of host-guest interactions for the co-assembly of BNA and dT_n (Figure. S1). Then, the thermal stability of the BNA_n-dT_n co-assemblies was examined using variable-temperature CD (VT-CD) experiments. All of the BNA_n-dT_n (n=6, 10 and 20) co-assemblies exhibited relatively high thermal stabilities compared to that of a regular (dA_n-dT_n) DNA duplex (melting temperature, T_m = 286.3 K (dA_6-dT_6), 294.2 K (dA_{10}-dT_{10}) and 318.8 K (dA_{20}-dT_{20}); Table S1),[47] which was due to the synergistic effect of WC base pairing, NDI-core aromatic π–π stacking and hydrophobic interactions of the n-butyl chain that stabilise the BNA_n-dT_n helical co-assembly (Figure. 2f). Moreover, the T_m values of BNA_n-dT_n were strongly dependent on the sequence length of dT_n (T_m = 343.1, 346.5 and 353.1 K for co-assemblies of BNA with dT_6, dT_{10} and dT_{20}, respectively). The observed dT_n sequence length dependent increase in the T_m values indicated that a longer dT_n sequence length improves the structural stability and integrity of the BNA_n-dT_n co-assembly.

To visualise the morphology of the BNA_n-dT_n co-assembly structures, field emission scanning electron microscopy (FESEM) measurements were performed by drop-casting their solutions (PBS, pH=7.4) onto a silicon (111) surface followed by washing with Milli-Q water to remove excess salt and drying under high vacuum at room temperature. BNA alone self-assembled into high aspect ratio 1D tapes that were micrometres in length and 20-60 nm wide (Figure. 3a). Under similar conditions, the mutually templated BNA_n-dT_n (n = 6, 10, 20) co-

assemblies formed 2D sheets with variable lateral dimensions that were dependent on the dT_n sequence length, as shown in Figure. 3b-d. The 2D BNA_6-dT_6 sheets exhibited an average lateral length and width of ~200 nm and ~500 nm, respectively. However, the average lateral length and width of BNA_{10}-dT_{10} were ~1.5 μm and ~400 nm, respectively, and for BNA_{20}:dT_{20}, these lateral dimensions were ~1 mM and 3 μm, respectively (Figure. 3b-d). These results were supported by the dynamic light scattering (DLS) data for BNA in the absence and presence of dT_n (Figure. S5). BNA alone exhibited aggregates with a relatively small size distribution of approximately 164 nm. Under similar conditions, the BNA_n-dT_n co-assemblies exhibited a size distribution with mean sizes of 396 nm, 531 nm and 615 nm, corresponding to the various dT_n lengths (n = 6, 10 and 20, respectively) (Figure. S5). Therefore, significant changes in the nanoscale morphology and DLS size distribution of the BNA_n-dT_n co-assemblies as well as the perfect correlation with the dT_n sequence length indicate the robustness of our methodology. In addition, we were able to construct and control extended BNA_n-dT_n co-assemblies in solution as well as in the form of nanostructures by varying the sequence length of dT_n. In a majority of the cases, the chiral molecular organisation observed in solution was lost in the corresponding nanostructures. Therefore, to confirm the chiral molecular packing within the 2D BNA_n-dT_n sheets, we performed thin film CD studies (Figure. S3). Interestingly, in agreement with the solution studies, the thin film CD spectra exhibited an intense negative ICD signal in both the band-II (220-260 nm) and band-I (300-420 nm) absorption regions for the NDI chromophore with λ_{max} at 400 nm, confirming the retention of chiral molecular packing within the 2D sheets. Moreover, the powder X-ray diffraction (PXRD) data of the 1D and 2D nanostructures of BNA and BNA_n-dT_n contained sharp diffraction signals, suggesting crystalline molecular organisation within the nanostructures (Figure. 3e and S5). Interestingly, the 2D sheets of the BNA_n-dT_n co-assemblies

exhibited new dT_n-sequence length dependent diffraction signals in the 2θ = 26º- 28º region, corresponding to the aromatic NDI-NDI π–π stacking distance. The 2D sheets of BNA_6-dT_6 exhibited diffraction signals at 2θ= 26.6º, which shifted upward as the dT_n sequence length increased (i.e., 27° for BNA_{10}:dT_{10} and 27.5° for BNA_{20}:dT_{20}). Therefore, the gradual decrease in the d-spacing values for the NDI-NDI π–π stacking as a function of the sequence length of dT_n (Table S2) indicates the formation of tighter packing of the BNA molecules within the BNA_n-dT_n co-assembly owing to increased cooperative interactions between the constituent partners supported by hydrophobic, aromatic π–π stacking and hydrogen bonding interactions. These structural insights into the BNA_n-dT_n co-assemblies inspired us to construct a field-effect transistor (FET) device and examine the charge transport characteristics of BNA in the presence and absence of dT_n.

2.3. FET characteristics of BNA and BNA_n-dT_n co-assembly structures

Transport measurements were performed on the self-assembled BNA and BNA_n-dT_n structures to understand the role of dT_n on the mutually template co-assembly and resulting BNA organisation (Figure. 3f). Bottom contact top gate FET structures were fabricated by introducing the supramolecular structures from the solution phase onto a benzocyclobutene (BCB) dielectric layer followed by coating the Au source-drain electrode (Figure. S6). All of the supramolecular structures exhibited typical n-type transport with μ_{FET} in the range of 10^{-3} $cm^2V^{-1}s^{-1}$ (Figure. 3f, Table S3 in Supplementary Section). It was observed that μ_{FET} scaled linearly with the dT_n sequence length (n = 6, 10, 20) used for the templated co-assembly, indicating that the transport variation is inherent to the co-assembly. From a microscopic point of view, the dT_n and BNA co-assembled structures exhibited a higher degree of crystallinity as the π-π stacking distance among the BNA stacks decreased (Figure. 3e). Therefore, BNA_n-dT_n exhibited tighter packing of

BNA with ordered lamellae, which is expected to promote charge transport with more tolerance towards defects and disorder.[74-75] Macroscopically, the molecular structure originating from the co-assembly of dT_n and BNA resulted in the formation of a 2D sheet-like structure, which is more tolerant to molecular disorder compared to 1D tapes obtained from pristine BNA (Figure. 3). The role of various nanostructure morphology on the transport at a dielectric-semiconductor interface can be elucidated by comparing the doping level of the 1D tapes and 2D sheets. For a capacitance of 4nF/cm^2, the doping levels were determined to be 10^9 for 1D tapes consisting of pristine BNA and 10^{11} for 2D sheets obtained from BNA_{20}-dT_{20}. A combination of all of these factors contributed to the better transport properties of the BNA_n-dT_n 2D sheets compared to those of the 1D tapes consisting of pristine BNA.

2.4. Chiroptical detection of Hg^{2+}

After successfully achieving the mutually templated co-assembly of BNA and dT_n with tuneable chiroptical, morphological and electronic properties, we investigated the selective disruption of the BNA_{10}-dT_{10} co-assembly with Hg^{2+} via T-Hg-T interactions to develop a versatile detection platform for the mercury ion (Figure. 4). By monitoring ICD intensity at 400 nm, the results from our preliminary investigations on thin films of BNA_{10}-dT_{10} in the absence and presence of Hg^{2+} ($Hg(ClO_4)_2.xH_2O$) are shown in Figure. 4a. Interestingly, the addition of Hg^{2+} (100 μM) to BNA_{10}-dT_{10} (110 μM) resulted in a significant reduction in the ICD signals in both the band II (220-260 nm) and band I (300-420 nm) regions of BNA (Figure. 4a *inset*). Moreover, in the presence of Hg^{2+}, a huge red shift (~38 nm) of the CD signal in the nucleobase absorption region (from λ_{max}= 252 nm to 290 nm) was observed, indicating the transformation of the BNA_{10}-dT_{10} helical co-assembly into a metallo-DNA duplex $[dT\text{-}Hg\text{-}dT]_{10}$ (Figure. 4a *inset*) and subsequent displacement of BNA.[76] Similar chiroptical response was observed in presence of CH_3Hg^+ which

confirmed the ability of the BNA_{10}-dT_{10} system to effectively detect organic mercury (Figure S8c). Therefore, the CD data indicated that BNA_{10}-dT_{10} disassembles in the presence of mercury ions owing to the formation of stable $[dT\text{-}Hg\text{-}dT]_{10}$ (Figure. 1). To assess the selectivity, perchlorate salts of Na^+, Mg^{2+}, K+, Ca^{2+}, Co^{3+}, Ni^{2+}, Cu^{2+}, Hg^{2+} and Pb^{2+} were tested at 100 μM concentrations in water (Figure. S8). Except for Hg^{2+}, the ICD signals of BNA_{10}-dT_{10} in the 250-420 nm region were unaffected by most of the tested metal ions, indicating a selective response towards Hg^{2+} due to preferential transformation of BNA_{10}-dT_{10} into $[dT\text{-}Hg\text{-}dT]_{10}$. To estimate the sensitivity of the detection, the ICD signal intensity of BNA_{10}-dT_{10} at 400 nm was monitored upon addition of various Hg^{2+} concentrations (0.1 nM to 50 μM) (Figure. 4b). The titration data revealed that Hg^{2+} concentrations up to 0.1 nM could be easily detected owing to a significant change in the ICD signal intensity. The binding constant of N-Hg-N was calculated from the binding isotherm curve fitting using the formula $1/\Delta CD = (1/b\Delta\varepsilon[G]_0[H]_0K_a) + (1/b\Delta\varepsilon[H]_0)$. The slope $(1/b\Delta\varepsilon[H]_0K_a) = 6.547\text{x } 10^{-11}$ and intercept $(1/b\Delta\varepsilon[H]_0) = 0.1144$ extracted from the linear fitted curve were used to calculated the binding constant which is found to be $K_a = 1.74\text{x}10^9$ M. Furthermore, the practical utility of the detection platform is demonstrated by measuring the levels of Hg^{2+} in simulated real sample (Figure S7). We performed CD measurements of samples containing tap water, well water, lake water and serum albumin with and without Hg^{2+} contamination employing BNA_{10}-dT_{10} chiral assembly in PBS buffer. Remarkably, all the Hg^{2+} (5 nM) contaminated samples exhibited significant and quantifiable change in the CD intensity of ~20% and 40% corresponding to 5 nM and 10 nM of Hg^{2+}, respectively. This study validated that BNA_n-dT_n is a robust system and practically viable platform for monitoring mercury in real samples without the interference from other biological or environmental constituents (Figure S7). Interestingly, the morphology study indicated that the addition of Hg^{2+} transformed the 2D sheets

of BNA_{10}-dT_{10} into 1D tapes, which may be due to the self-assembled structures of displaced BNA (Figure. 4c). Overall, the change in the ICD signals and morphology (2D to 1D) owing to transformation of BNA_{10}-dT_{10} into $[dT\text{-}Hg\text{-}dT]_{10}$ in the presence of Hg^{2+} can be effectively used to detect the metal ion at sub-nanomolar concentrations.

2.5. Conductometric detection of CH_3Hg^+.

The ability to tune the transport property of BNA through BNA_n-dT_n co-assembly was further utilised to develop electrical devices for a sensing application (Figure. 5). As demonstrated, Hg^{2+} drives the transformation of BNA_{10}-dT_{10} into a metal-DNA duplex $[dT\text{-}Hg\text{-}dT]_{10}$ owing to the preferential selectivity of Hg^{2+} to thymine (T). This selective transformation, which involves the displacement of BNA by Hg^{2+}/CH_3Hg^+, was employed to design an ultrasensitive detection platform. The device structure involved fabrication of lateral two terminal devices (L = 60 μm, W = 1 mm) to monitor the conductivity (σ) variation of the BNA_{10}-dT_{10} co-assembled structures upon the addition of different organic and inorganic forms Hg^{2+} at different concentrations (Figure. 5a *inset)*. A typical σ of ~ 10^{-6} S/cm and current density (J at 5 V) as high as 5×10^3 A/m^2 were obtained for the BNA_{10}-dT_{10} active layer (Figure. 5a). For the sensing measurement, 20 μL of different forms of mercury (CH_3Hg^+ or Hg^{2+}) salt solution in Milli-Q water were introduced onto the co-assembled active layer. Upon addition of the salt solution onto the lateral device with co-assembled active layer, a decrease in the current density was observed (Figure. 5a). This decrease in the observed conductivity could originate from a number of external factors like degradation of the device due to introduction of water or it could be due to the inherent modification of the active semiconducting layer. Hence, control measurements were performed on different metallic salt solutions of Na^+, K^+ (20 μL of 0.1 μM solution) on similar devices. Interestingly, the introduction of Na^+, K^+ solutions on the lateral devices resulted in an increase

in conductivity by an order of magnitude, indicating that no inherent degradation of the device is observed upon addition of the salt solution (Figure S9). Furthermore, the increase in conductivity can be related to the additional ionic channels created for conduction in these devices. In addition, it was also observed that the conductivity of the devices were restored to the original value when the salt treated (Na^+, K^+) devices were washed with water. These control measurements indicate that for devices where mercury ions were added to the BNA_{10}-dT_{10} active layer, the decrease in J and σ can then be correlated to the assembly transformation. The preferential binding of mercury ions to T's (dT_{10}) break the co-assembly of BNA_{10}-dT_{10}, which results in the formation of $[dT\text{-}Hg\text{-}dT]_{10}$ and release of pristine BNA molecules. Furthermore, it was also observed that the extent of dissociation in the co-assembled nanostructure is proportional to the amount of Hg^{2+}/ CH_3Hg^+ added. Therefore this BNA_n-dT_n platform is capable of detecting mercury ions either from inorganic (Hg^{2+}) or organic (CH_3Hg^+) sources with high selectivity and sensitivity, although do not distinguish the two types. Notably, appreciable variation in the conductivity was observed for Hg^{2+} concentrations as low as 0.1 nM, which dictates the lower detection limit of our conductometric-based mercury sensing device. We defined the sensitivity of the device (χ) by the plotting the $\sigma_{before}/\sigma_{after}$ ratio as a function of the added Hg^{2+} concentration (Figure. 5b). To confirm that the observed variation in the conductivity and current density was directly related to the change in the assembly structure, we performed conductive AFM measurement (CAFM) on a single sheet (Figure. 5c). CAFM measurements on the 2D sheet of the BNA_{10}-dT_{10} co-assembly indicated an order of magnitude decrease in the conductivity when 0.1 μM Hg^{2+} was added. The CAFM measurements provide a direct evidence of Hg^{2+} induced assembly transformation from BNA_{10}-dT_{10} to the $[dT\text{-}Hg\text{-}dT]_{10}$ metallo-DNA duplex as the factor responsible for the observed changes in the bulk conductivity.

3. CONCLUSIONS

We developed a novel nanoarchitectonics based on the mutually templated co-assembly (BNA_n-dT_n) of an organic semiconductor (BNA) and deoxyribo-oligothymidine (dT_n) for the selective and ultrasensitive detection of aqueous mercury. The metal ion-assisted selective transformation of BNA_{10}-dT_{10} into a metallo-DNA duplex $[dT\text{-}Hg\text{-}dT]_{10}$ was used as a chiroptical and conductivity based sensor platform for mercury detection. Interesting correlation in terms of the dT_n sequence length and the stability, integrity and functional properties of the BNA_n-dT_n co-assembly was obtained from a range of microscopic and spectroscopic measurements. This dynamic self-assembly property is utilized for a chiroptical and conductivity-based sensor which exhibited sub-nanomolar sensitivity (0.1 nM or 0.02 ppb) towards mercury ions (inorganic and organometallic forms) in water. Such a design strategy involving mutual templated small molecule and ssDNA/deoxyribo-oligonucleotide co-assembly is expected to aid in the development of new templated DNA nanoarchitectonics approaches to design potentially useful bio-optoelectronics and sensor application platforms.

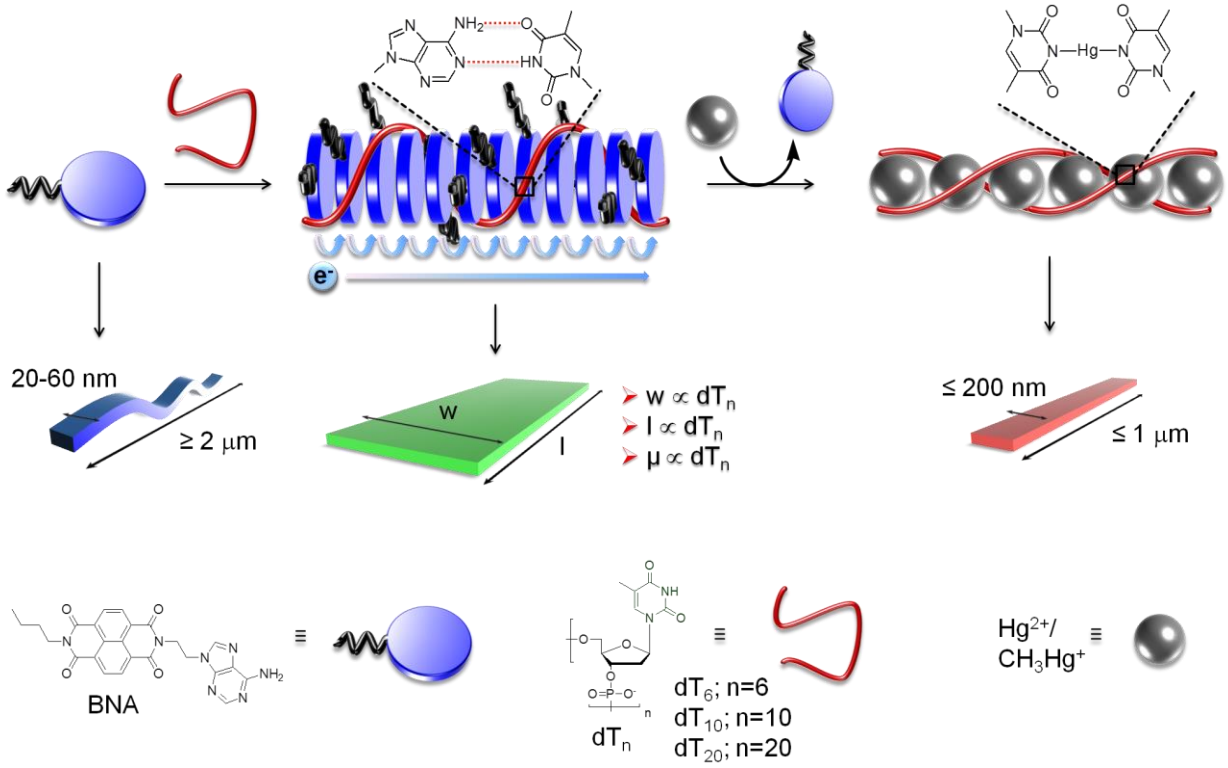

Figure 1. Schematic illustration of the proposed nanoarchitectonics of BNA and dT_n Co-assembly as well as the corresponding molecular structures. Molecular packing model for the BNA_n-dT_n mutually templated co-assembly via complementary Watson-Crick (WC) A-T hydrogen bonding interactions. In addition, the mutually templated co-assembly driven electron hopping among the stacked BNA molecules as well as the mercury mediated disassembly and transformation of BNA_n-dT_n into a metallo-DNA duplex $[dT\text{-}Hg\text{-}dT]_n$ are shown. Schematic representation of the corresponding morphology of the self-assembled BNA, BNA_n-dT_n co-assembly and $[dT\text{-}Hg\text{-}dT]_n$ along with their lateral dimensions (l= length, w= width). The 2D lateral dimensions and conductivity (μ) of the resulting BNA_n-dT_n co-assembled structures were directly proportional to the length of the dT_n used. Molecular structures and–corresponding pictorial representation of BNA, dT_n and Hg^{2+}/CH_3Hg^+.

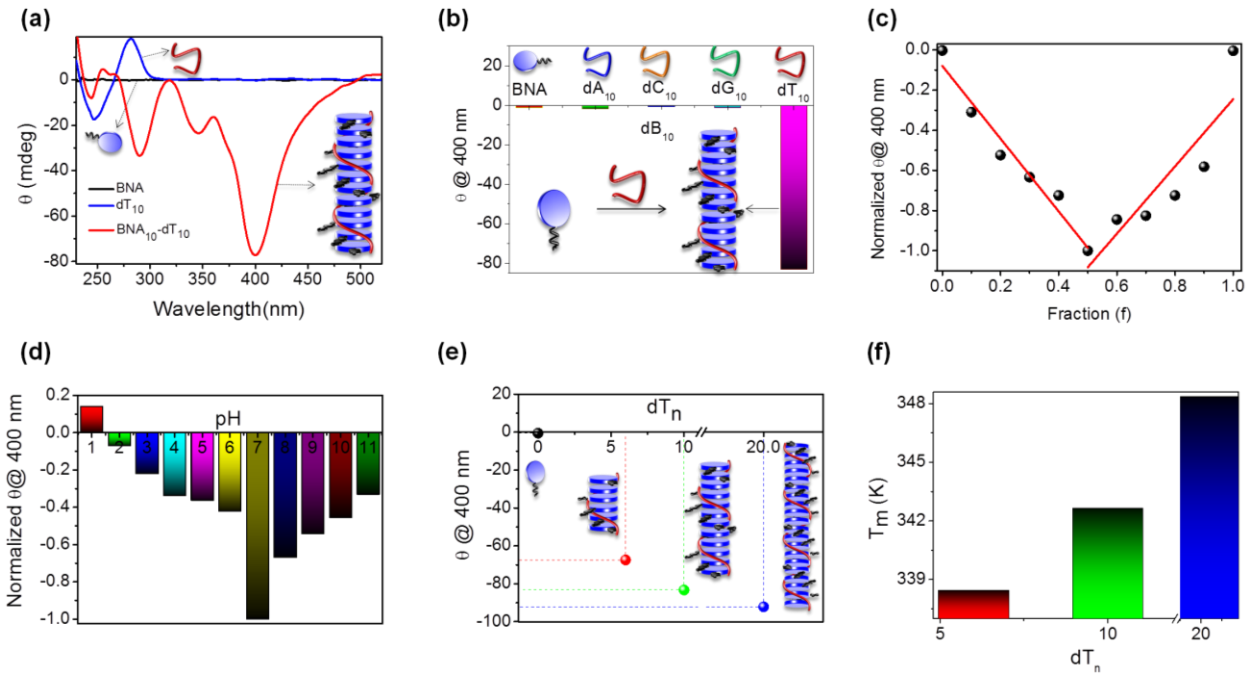

Figure 2. Circular dichroism (CD) spectroscopic characterisation of BNA and BNA_n-dT_n co-assembly. (a) CD spectra of BNA (100 μM), dT_{10} (10 μM) and BNA_{10}-dT_{10} (1:1, BNA:T) in PBS buffer (10 mM, pH = 7, contain 5% DMSO) at 293 K. *Inset:* pictorial representations of BNA, dT_{10} and BNA_{10}-dT_{10} with respective spectra. (b) Columnar graph comparison of ICD intensity at 400 nm for BNA in the presence of different deoxyoligonucleotides (dB_{10}) ([BNA]= 100 μM, [dB_{10}]= 10 μM). Schematic representation of the formation of the mutually templated co-assembly of BNA_{10}-dT_{10} via selective A-T base pairing interactions. (c) ICD Job plot monitored at 400 nm as a function of the fraction of BNA (f) in BNA_{10}-dT_{10} ([BNA]+[dT_{10}]= 110 μM with f= [BNA]/110 mM). (d) pH dependent ICD spectral studies of BNA_{10}-dT_{10} (BNA:T (1:1)) at 400 nm and 293 K. (e) and (f) dT_n (n=6, 10 and 20) sequence length dependent ICD signal intensity (pictorial representation of corresponding dT_n length dependent BNA_n-dT_n co-assembly) and respective ICD melting temperature values of BNA_n-dT_n (BNA:T (1:1)) monitored at 400 nm respectively.

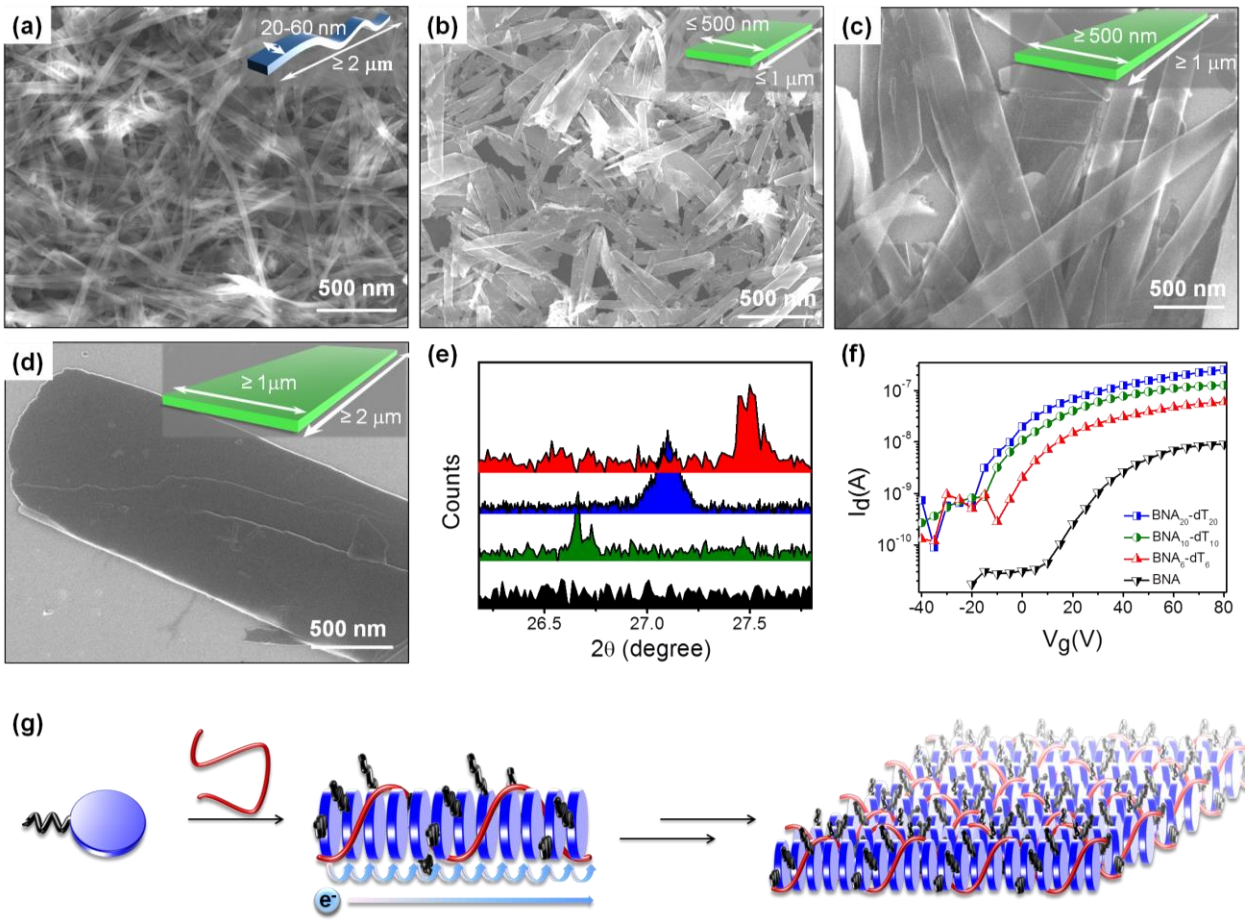

Figure 3. Morphological and structural analysis of the BNA and BNA_n-dT_n co-assemblies. FESEM micrographs of BNA (a), BNA_6-dT_6 (b), BNA_{10}-dT_{10} (c) and BNA_{20}-dT_{20} (d). *Inset:* schematic representation of respective structures with their lateral dimensions. (e) PXRD diffraction patterns in the aromatic π–stacking region ($2\theta = 26^{\circ}$-27°). (f) Typical transconductance plots for the different self-assembled BNA and BNA_n-dT_n co-assembly structures. (g) Schematic representation of mutually templated BNA_n-dT_n co-assembly into conducting 2D organisation.

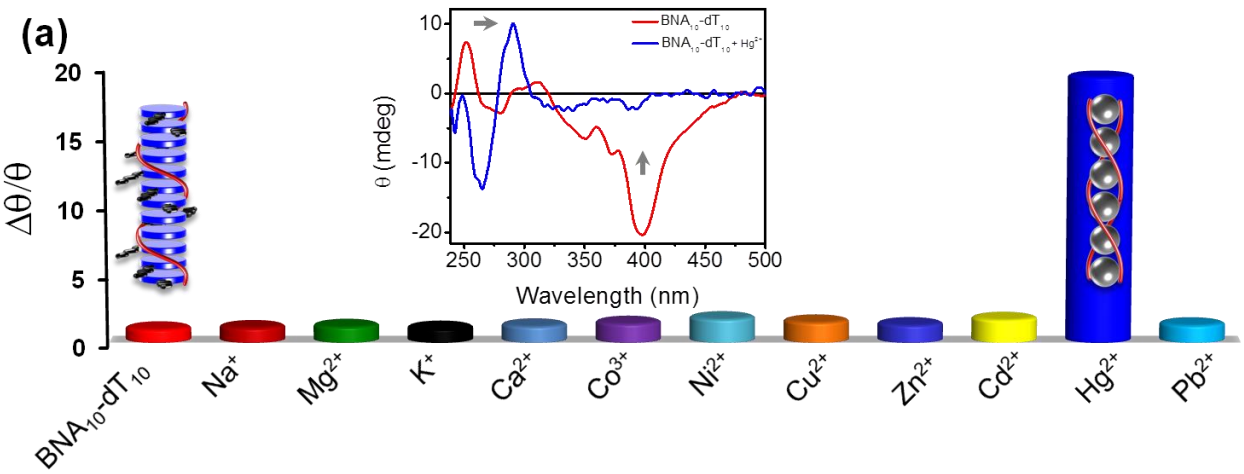
(a)
Δθ/θ
20
15
10
5
0
BNA10-dT10
Na+
Mg2+
K+
Ca2+
Co3+
Ni2+
Cu2+
Zn2+
Cd2+
Hg2+
Pb2+
θ (mdeg)
Wavelength (nm)
BNA10-dT10
BNA10-dT10 + Hg2+

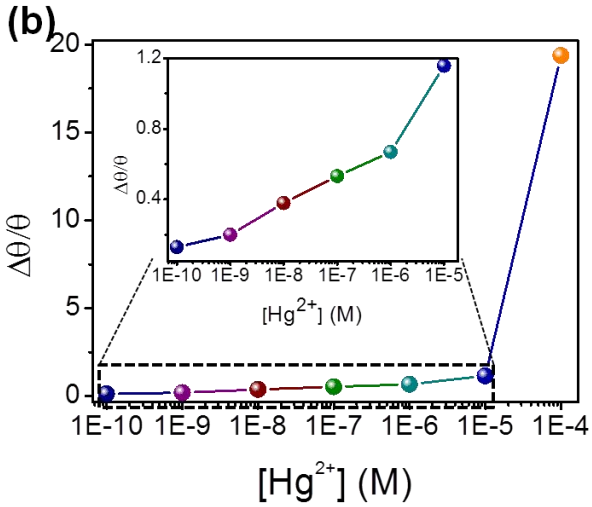
(b)
Δθ/θ
[Hg2+] (M)
1E-10 1E-9 1E-8 1E-7 1E-6 1E-5 1E-4

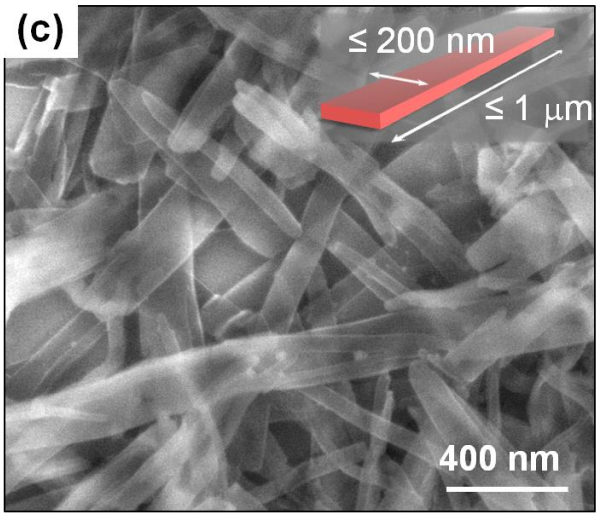
(c)
≤ 200 nm
≤ 1 μm
400 nm

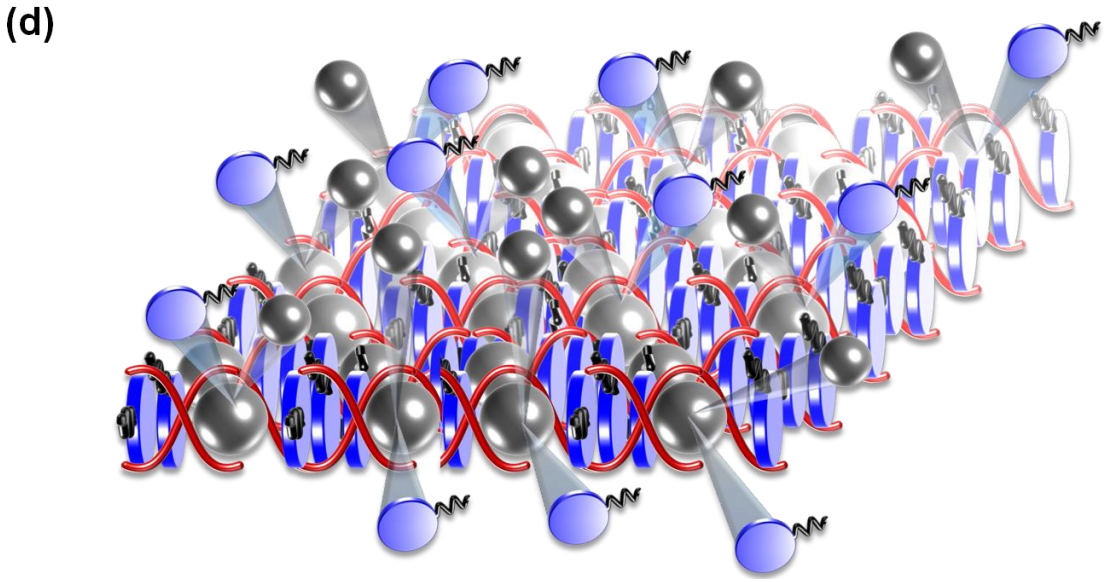
(d)

Figure 4. Chiroptical sensing of Hg^{2+}. **(**a) Relative thin film ICD intensity of BNA_{10}-dT_{10} at 400 nm in the presence of various metal ions (where $[M^{n+}]$= 100 μM, $\Delta\theta = \theta_0 - \theta$; θ_0 and θ are ICD intensity values at 400 nm before and after addition of metal ions, respectively). *Inset:* thin film CD spectra of BNA_{10}-dT_{10} before and after addition of Hg^{2+} and schematic representation of the respective assemblies. (b) Relative thin film ICD intensity of BNA_{10}-dT_{10} at 400 nm as a function of added $[Hg^{2+}]$. *Inset:* enhanced selected spectral region of dotted line box (0.1 nM to 10 μM). (c) FESEM micrograph of BNA_{10}-dT_{10} after the addition of Hg^{2+}. (d) Schematic representation of Hg^{2+} induced displacement of BNA from the BNA_n-dT_n 2D assembly via formation of a metallo-DNA duplex $[dT\text{-}Hg\text{-}dT]_n$ and self-assembled BNA 1D tapes, as shown in c.

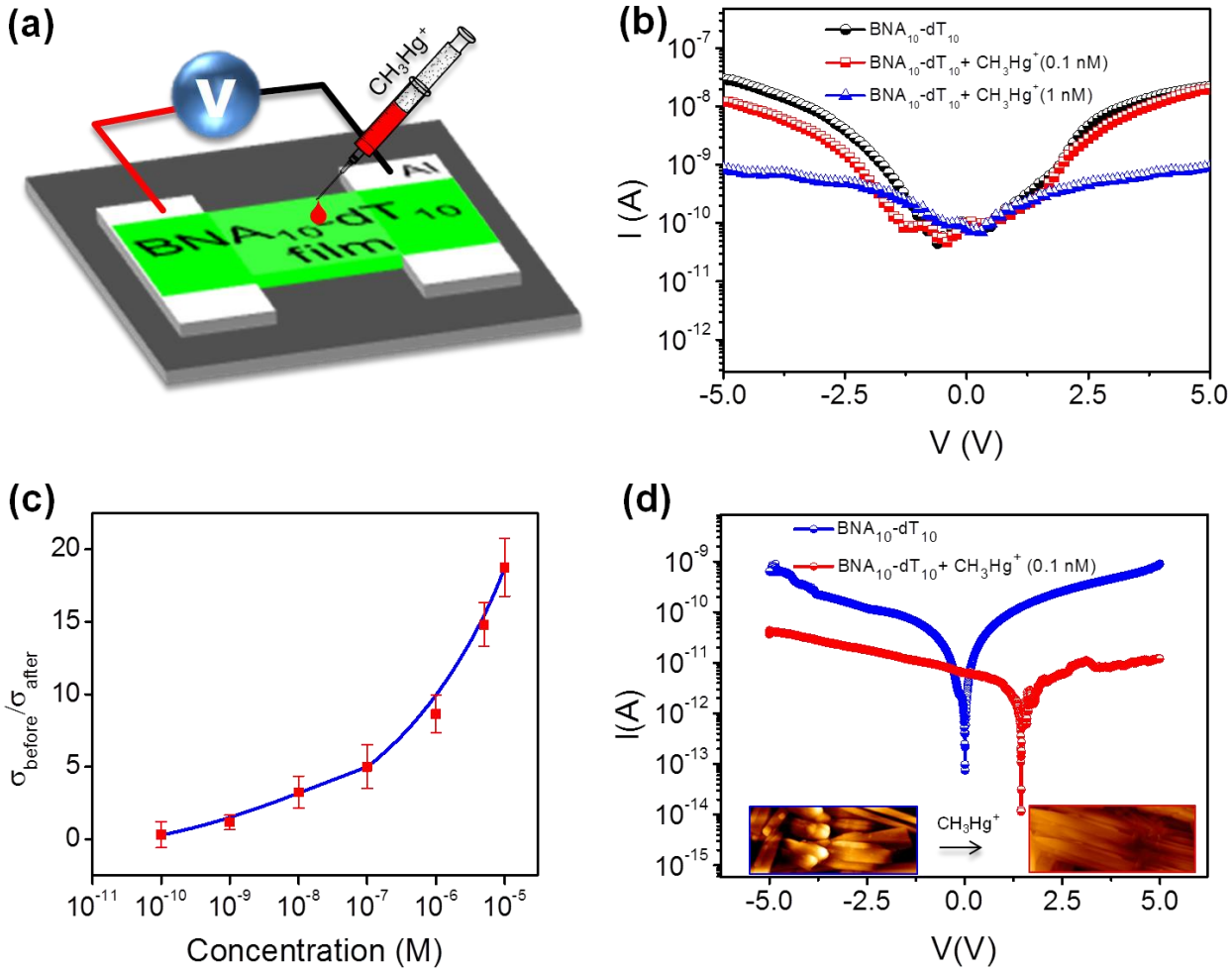

Figure 5. Conductometric sensing of CH_3Hg^+. (a) Schematic representation of CH_3Hg^+ detection device structure. (b) BNA_{10}-dT_{10} device response before and after addition of different CH_3Hg^+ concentrations (0.1 nM and 0.5 mM). (c) CH_3Hg^+ sensitivity study based on conductometric measurements obtained for different concentrations of CH_3Hg^+ ions. (d) Conductive AFM (CAFM) measurements of an individual 2D sheet of BNA_{10}-dT_{10} confirmed the change in the assembly and conductivity upon addition of CH_3Hg^+ ions, this further supports the data from the bulk measurements.

ASSOCIATED CONTENT

Supporting Information. Detailed experimental methods and additional characterization data. This material is available free of charge via the Internet at http://pubs.acs.org.

AUTHOR INFORMATION

Corresponding Author

*E-mail: tgraju@jncasr.ac.in

Present Addresses

‡ Optoelectronics Group, Cavendish Laboratory, University of Cambridge, JJ Thomson Avenue, CB3 0HE

Notes

The authors declare no competing financial interest.

ACKNOWLEDGMENT

Authors thank Prof. C. N. R. Rao FRS for constant support and encouragement, JNCASR, Department of Biotechnology (DBT)-(Nanotechnology Special Task force grant BT/PR10263/NNT/28/711/2013) and DST Nano Mission, India for financial support, Prof. K. S. Narayan, JNCASR for providing facilities for conductometric measurements and discussions regarding the device measurements, Dr. N. Nagarjun, for help in the synthesis of a molecule, SPS acknowledges CSIR-India for research fellowship. We thank Prof. Sir Richard Friend, University of Cambridge for reading the manuscript and providing critical comments.

REFERENCES

(1) Lamborg, C. H.; Hammerschmidt, C. R.; Bowman, K. L.; Swarr, G. J.; Munson, K. M.; Ohnemus, D. C.; Lam, P. J.; Heimburger, L.-E.; Rijkenberg, M. J. A.; Saito, M. A., A Global Ocean Inventory of Anthropogenic Mercury Based on Water Column Measurements. *Nature* **2014,** *512*, 65-68.

(2) Kim, H. N.; Ren, W. X.; Kim, J. S.; Yoon, J., Fluorescent and Colorimetric Sensors for Detection of Lead, Cadmium, and Mercury Ions. *Chem. Soc. Rev.* **2012,** *41*, 3210-3244.

(3) Nicholson, J. K.; Kendall, M. D.; Osborn, D., Cadmium and Mercury Nephrotoxicity. *Nature* **1983,** *304*, 633-635.

(4) UNEP, Global Mercury Assessment 2013: Sources, Emissions, Releases and Environmental Transport *UNEP Chemicals Branch,Geneva* **2013**, Switzerland.

(5) Nolan, E. M.; Lippard, S. J., Tools and Tactics for the Optical Detection of Mercuric Ion. *Chem. Rev.* **2008,** *108*, 3443-3480.

(6) Jensen, S.; Jernelov, A., Biological Methylation of Mercury in Aquatic Organisms. *Nature* **1969,** *223*, 753-754.

(7) Renzoni, A.; Zino, F.; Franchi, E., Mercury Levels Along the Food Chain and Risk for Exposed Populations. *Environ. Res.* **1998,** *77*, 68-72.

(8) Ono, A.; Togashi, H., Highly Selective Oligonucleotide-Based Sensor for Mercury(II) in Aqueous Solutions. *Angew. Chem., Int. Ed. Engl.* **2004,** *43*, 4300-4302.

(9) Kim, I. B.; Bunz, U. H., Modulating the Sensory Response of a Conjugated Polymer by Proteins: An Agglutination Assay for Mercury Ions in Water. *J. Am. Chem. Soc.* **2006,** *128*, 2818-2819.

(10) Chen, L.; Fu, X.; Lu, W.; Chen, L., Highly Sensitive and Selective Colorimetric Sensing of Hg^{2+} Based on the Morphology Transition of Silver Nanoprisms. *ACS Appl. Mater. Interfaces* **2013,** *5*, 284-290.

(11) Chen, L.; Li, J.; Chen, L., Colorimetric Detection of Mercury Species Based on Functionalized Gold Nanoparticles. *ACS Appl. Mater. Interfaces* **2014,** *6*, 15897-15904.

(12) Xu, S.; Chen, L.; Li, J.; Guan, Y.; Lu, H., Novel Hg^{2+}-Imprinted Polymers Based on Thymine–Hg^{2+}–Thymine Interaction for Highly Selective Preconcentration of Hg^{2+} in Water Samples. *J. Hazard. Mater.* **2012,** *237–238*, 347-354.

(13) Lou, T.; Chen, Z.; Wang, Y.; Chen, L., Blue-to-Red Colorimetric Sensing Strategy for Hg^{2+} and Ag^{+} Via Redox-Regulated Surface Chemistry of Gold Nanoparticles. *ACS Appl. Mater. Interfaces* **2011,** *3*, 1568-1573.

(14) Liu, J.; Lu, Y., Rational Design of "Turn-on" Allosteric Dnazyme Catalytic Beacons for Aqueous Mercury Ions with Ultrahigh Sensitivity and Selectivity. *Angew. Chem. Int. Ed.* **2007,** *46*, 7587-7590.

(15) Wegner, S. V.; Okesli, A.; Chen, P.; He, C., Design of an Emission Ratiometric Biosensor from Merr Family Proteins: A Sensitive and Selective Sensor for Hg^{2+}. *J. Am. Chem. Soc.* **2007,** *129*, 3474-3475.

(16) Dave, N.; Chan, M. Y.; Huang, P. J.; Smith, B. D.; Liu, J., Regenerable DNA-Functionalized Hydrogels for Ultrasensitive, Instrument-Free Mercury(II) Detection and Removal in Water. *J. Am. Chem. Soc.* **2010,** *132*, 12668-12673.

(17) Loe-Mie, F.; Marchand, G.; Berthier, J.; Sarrut, N.; Pucheault, M.; Blanchard-Desce, M.; Vinet, F.; Vaultier, M., Towards an Efficient Microsystem for the Real-Time Detection and Quantification of Mercury in Water Based on a Specifically Designed Fluorogenic Binary Task-Specific Ionic Liquid. *Angew. Chem., Int. Ed. Engl.* **2010,** *49*, 424-427.

(18) Ye, B. C.; Yin, B. C., Highly Sensitive Detection of Mercury(II) Ions by Fluorescence Polarization Enhanced by Gold Nanoparticles. *Angew. Chem., Int. Ed. Engl.* **2008,** *47*, 8386-8389.

(19) Han, D.; Lim, S. Y.; Kim, B. J.; Piao, L.; Chung, T. D., Mercury(II) Detection by Sers Based on a Single Gold Microshell. *Chem. Commun.* **2010,** *46*, 5587-5589.

(20) Esmaielzadeh Kandjani, A.; Sabri, Y. M.; Mohammad-Taheri, M.; Bansal, V.; Bhargava, S. K., Detect, Remove and Reuse: A New Paradigm in Sensing and Removal of Hg (Ii) from Wastewater Via Sers-Active Zno/Ag Nanoarrays. *Environ. Sci. Technol.* **2015,** *49*, 1578-1584.

(21) Wen, S.; Zeng, T.; Liu, L.; Zhao, K.; Zhao, Y.; Liu, X.; Wu, H. C., Highly Sensitive and Selective DNA-Based Detection of Mercury(II) with Alpha-Hemolysin Nanopore. *J. Am. Chem. Soc.* **2011,** *133*, 18312-18317.

(22) Xue, X.; Wang, F.; Liu, X., One-Step, Room Temperature, Colorimetric Detection of Mercury (Hg^{2+}) Using DNA/Nanoparticle Conjugates. *J. Am. Chem. Soc.* **2008,** *130*, 3244-3245.

(23) Zheng, P.; Li, M.; Jurevic, R.; Cushing, S. K.; Liu, Y.; Wu, N., A Gold Nanohole Array Based Surface-Enhanced Raman Scattering Biosensor for Detection of Silver(I) and Mercury(II) in Human Saliva. *Nanoscale* **2015,** *7*, 11005-11012.

(24) Du, J.; Jiang, L.; Shao, Q.; Liu, X.; Marks, R. S.; Ma, J.; Chen, X., Colorimetric Detection of Mercury Ions Based on Plasmonic Nanoparticles. *Small* **2013,** *9*, 1467-1481.

(25) Mitra, A.; Mittal, A. K.; Rao, C. P., Carbohydrate Assisted Fluorescence Turn-on Gluco-Imino-Anthracenyl Conjugate as a Hg(II) Sensor in Milk and Blood Serum Milieu. *Chem. Commun.* **2011,** *47*, 2565-2567.

(26) Areti, S.; Hinge, V. K.; Rao, C. P., Pyrenyl-Imino-C2-Glucosyl Conjugate: Synthesis, Characterization, and Ratiometric and Reversible Off–on Receptor for Hg^{2+}. *Carbohydr. Res.* **2014,** *399*, 64-69.

(27) Dessingou, J.; Tabbasum, K.; Mitra, A.; Hinge, V. K.; Rao, C. P., Lower Rim 1,3-Di{4-Antipyrine}Amide Conjugate of Calix[4]Arene: Synthesis, Characterization, and Selective Recognition of Hg^{2+} and Its Sensitivity toward Pyrimidine Bases. *J. Org. Chem.* **2012,** *77*, 1406-1413.

(28) Bandela, A.; Chinta, J. P.; Rao, C. P., Role of the Conformational Changes Brought in the Arms of the 1,3-Di-Capped Conjugate of Calix[4]Arene (L) in Turning on the Fluorescence of L by Hg^{2+}. *Dalton Trans.* **2011,** *40*, 11367-11370.

(29) Mitra, A.; Rao, C. P., Naked Eye Sensing of Hg^{2+} Using Glucose Based Anthracenyl Imino Derivative. *Trends Carbohydr. Res.* **2011,** *3*, 44-46.

(30) Mor-Piperberg, G.; Tel-Vered, R.; Elbaz, J.; Willner, I., Nanoengineered Electrically Contacted Enzymes on DNA Scaffolds: Functional Assemblies for the Selective Analysis of Hg^{2+} Ions. *J. Am. Chem. Soc.* **2010,** *132*, 6878-6879.

(31) Zeng, T.; Li, T.; Li, Y.; Liu, L.; Wang, X.; Liu, Q.; Zhao, Y.; Wu, H. C., DNA-Based Detection of Mercury(II) Ions through Characteristic Current Signals in Nanopores with High Sensitivity and Selectivity. *Nanoscale* **2014,** *6*, 8579-8584.

(32) Lin, Z. H.; Zhu, G.; Zhou, Y. S.; Yang, Y.; Bai, P.; Chen, J.; Wang, Z. L., A Self-Powered Triboelectric Nanosensor for Mercury Ion Detection. *Angew. Chem., Int. Ed. Engl.* **2013,** *52*, 5065-5069.

(33) Zhang, T.; Cheng, Z.; Wang, Y.; Li, Z.; Wang, C.; Li, Y.; Fang, Y., Self-Assembled 1-Octadecanethiol Monolayers on Graphene for Mercury Detection. *Nano Lett.* **2010,** *10*, 4738-4741.

(34) Cho, E. S.; Kim, J.; Tejerina, B.; Hermans, T. M.; Jiang, H.; Nakanishi, H.; Yu, M.; Patashinski, A. Z.; Glotzer, S. C.; Stellacci, F.; Grzybowski, B. A., Ultrasensitive Detection of Toxic Cations through Changes in the Tunnelling Current across Films of Striped Nanoparticles. *Nat. Mater.* **2012,** *11*, 978-985.

(35) Knopfmacher, O.; Hammock, M. L.; Appleton, A. L.; Schwartz, G.; Mei, J.; Lei, T.; Pei, J.; Bao, Z., Highly Stable Organic Polymer Field-Effect Transistor Sensor for Selective Detection in the Marine Environment. *Nat. Commun.* **2014,** *5*, 2954.

(36) Katz, S., The Reversible Reaction of Hg (Ii) and Double-Stranded Polynucleotides a Step-Function Theory and Its Significance. *Biochim. Biophys. Acta* **1963,** *68*, 240-253.

(37) Katz, S., The Reversible Reaction of Sodium Thymonucleate and Mercuric Chloride. *J. Am. Chem. Soc.* **1952,** *74*, 2238-2245.

(38) Thomas, C. A., The Interaction of $Hgcl_2$ with Sodium Thymonucleate. *J. Am. Chem. Soc.* **1954,** *76*, 6032-6034.

(39) Joseph, R.; Ramanujam, B.; Acharya, A.; Khutia, A.; Rao, C. P., Experimental and Computational Studies of Selective Recognition of Hg^{2+} by Amide Linked Lower Rim 1,3-Dibenzimidazole Derivative of Calix[4]Arene: Species Characterization in Solution and That in the Isolated Complex, Including the Delineation of the Nanostructures. *J. Org. Chem.* **2008,** *73*, 5745-5758.

(40) Huang, C. C.; Yang, Z.; Lee, K. H.; Chang, H. T., Synthesis of Highly Fluorescent Gold Nanoparticles for Sensing Mercury(II). *Angew. Chem., Int. Ed. Engl.* **2007,** *46*, 6824-6828.

(41) Lee, J. S.; Han, M. S.; Mirkin, C. A., Colorimetric Detection of Mercuric Ion (Hg^{2+}) in Aqueous Media Using DNA-Functionalized Gold Nanoparticles. *Angew. Chem. Int. Ed.* **2007,** *46*, 4093-4096.

(42) Li, D.; Wieckowska, A.; Willner, I., Optical Analysis of Hg^{2+} Ions by Oligonucleotide-Gold-Nanoparticle Hybrids and DNA-Based Machines. *Angew. Chem., Int. Ed. Engl.* **2008,** *47*, 3927-3931.

(43) Zhu, Y.; Xu, L.; Ma, W.; Xu, Z.; Kuang, H.; Wang, L.; Xu, C., A One-Step Homogeneous Plasmonic Circular Dichroism Detection of Aqueous Mercury Ions Using Nucleic Acid Functionalized Gold Nanorods. *Chem. Commun.* **2012,** *48*, 11889-11891.

(44) Zhang, L.; Li, T.; Li, B.; Li, J.; Wang, E., Carbon Nanotube-DNA Hybrid Fluorescent Sensor for Sensitive and Selective Detection of Mercury(II) Ion. *Chem. Commun.* **2010,** *46*, 1476-1478.

(45) Helwa, Y.; Dave, N.; Froidevaux, R.; Samadi, A.; Liu, J., Aptamer-Functionalized Hydrogel Microparticles for Fast Visual Detection of Mercury(II) and Adenosine. *ACS Appl. Mater. Interfaces* **2012,** *4*, 2228-2233.

(46) Xu, H.; Zhu, X.; Ye, H.; Yu, L.; Liu, X.; Chen, G., A Simple "Molecular Beacon"-Based Fluorescent Sensing Strategy for Sensitive and Selective Detection of Mercury (II). *Chem. Commun.* **2011,** *47*, 12158-12160.

(47) Narayanaswamy, N.; Suresh, G.; Priyakumar, U. D.; Govindaraju, T., Double Zipper Helical Assembly of Deoxyoligonucleotides: Mutual Templating and Chiral Imprinting to Form Hybrid DNA Ensembles. *Chem. Commun.* **2015,** *51*, 5493-5496.

(48) Hannah, K. C.; Armitage, B. A., DNA-Templated Assembly of Helical Cyanine Dye Aggregates: A Supramolecular Chain Polymerization. *Acc. Chem. Res.* **2004,** *37*, 845-853.

(49) Ruiz-Carretero, A.; Janssen, P. G.; Kaeser, A.; Schenning, A. P., DNA-Templated Assembly of Dyes and Extended Pi-Conjugated Systems. *Chem. Commun.* **2011,** *47*, 4340-4347.

(50) Aono, M.; Ariga, K., The Way to Nanoarchitectonics and the Way of Nanoarchitectonics. *Adv. Mater.* **2016,** *28*, 989-992.

(51) Ariga, K.; Ji, Q. M.; Nakanishi, W.; Hill, J. P.; Aono, M., Nanoarchitectonics: A New Materials Horizon for Nanotechnology. *Mater. Horiz.* **2015,** *2*, 406-413.

(52) Nakanishi, W.; Minami, K.; Shrestha, L. K.; Ji, Q.; Hill, J. P.; Ariga, K., Bioactive Nanocarbon Assemblies: Nanoarchitectonics and Applications. *Nano Today* **2014,** *9*, 378-394.

(53) Govindaraju, T.; Avinash, M. B., Two-Dimensional Nanoarchitectonics: Organic and Hybrid Materials. *Nanoscale* **2012,** *4*, 6102-6117.

(54) Pandeeswar, M.; Khare, H.; Ramakumar, S.; Govindaraju, T., Crystallographic Insight-Guided Nanoarchitectonics and Conductivity Modulation of an N-Type Organic Semiconductor through Peptide Conjugation. *Chem. Commun.* **2015,** *51*, 8315-8318.

(55) Avinash, M. B.; Swathi, K.; Narayan, K. S.; Govindaraju, T., Molecular Architectonics of Naphthalenediimides for Efficient Structure-Property Correlation. *ACS Appl. Mater. Interfaces* **2016,** *8*, 8678-8685.

(56) Pandeeswar, M.; Senanayak, S. P.; Narayan, K. S.; Govindaraju, T., Multi-Stimuli-Responsive Charge-Transfer Hydrogel for Room-Temperature Organic Ferroelectric Thin-Film Devices. *J. Am. Chem. Soc.* **2016,** *138*, 8259-8268.

(57) Avinash, M. B.; Govindaraju, T., Amino Acid Derivatized Arylenediimides: A Versatile Modular Approach for Functional Molecular Materials. *Adv. Mater.* **2012,** *24*, 3905-3922.

(58) Dwivedi, A. K.; Pandeeswar, M.; Govindaraju, T., Assembly Modulation of Pdi Derivative as a Supramolecular Fluorescence Switching Probe for Detection of Cationic Surfactant and Metal Ions in Aqueous Media. *ACS Appl. Mater. Interfaces* **2014,** *6*, 21369-21379.

(59) Houlton, A.; Pike, A. R.; Angel Galindo, M.; Horrocks, B. R., DNA-Based Routes to Semiconducting Nanomaterials. *Chem. Commun.* **2009**, 1797-1806.

(60) de la Escosura, A.; Janssen, P. G.; Schenning, A. P.; Nolte, R. J.; Cornelissen, J. J., Encapsulation of DNA-Templated Chromophore Assemblies within Virus Protein Nanotubes. *Angew. Chem., Int. Ed. Engl.* **2010,** *49*, 5335-5338.

(61) Varghese, R.; Wagenknecht, H. A., DNA as a Supramolecular Framework for the Helical Arrangements of Chromophores: Towards Photoactive DNA-Based Nanomaterials. *Chem. Commun.* **2009**, 2615-2624.

(62) Teo, Y. N.; Kool, E. T., DNA-Multichromophore Systems. *Chem. Rev.* **2012,** *112*, 4221-4245.

(63) Bandy, T. J.; Brewer, A.; Burns, J. R.; Marth, G.; Nguyen, T.; Stulz, E., DNA as Supramolecular Scaffold for Functional Molecules: Progress in DNA Nanotechnology. *Chem. Soc. Rev.* **2011,** *40*, 138-148.

(64) Malinovskii, V. L.; Wenger, D.; Haner, R., Nucleic Acid-Guided Assembly of Aromatic Chromophores. *Chem. Soc. Rev.* **2010,** *39*, 410-422.

(65) Berger, O.; Adler-Abramovich, L.; Levy-Sakin, M.; Grunwald, A.; Liebes-Peer, Y.; Bachar, M.; Buzhansky, L.; Mossou, E.; Forsyth, V. T.; Schwartz, T.; Ebenstein, Y.; Frolow, F.; Shimon, L. J. W.; Patolsky, F.; Gazit, E., Light-Emitting Self-Assembled Peptide Nucleic Acids Exhibit Both Stacking Interactions and Watson-Crick Base Pairing. *Nat. Nanotechnol.* **2015,** *10*, 353-360.

(66) Castronovo, M.; Lucesoli, A.; Parisse, P.; Kurnikova, A.; Malhotra, A.; Grassi, M.; Grassi, G.; Scaggiante, B.; Casalis, L.; Scoles, G., Two-Dimensional Enzyme Diffusion in Laterally Confined DNA Monolayers. *Nat. Commun.* **2011,** *2*, 297.

(67) Di Michele, L.; Varrato, F.; Kotar, J.; Nathan, S. H.; Foffi, G.; Eiser, E., Multistep Kinetic Self-Assembly of DNA-Coated Colloids. *Nat. Commun.* **2013,** *4*.

(68) Yonamine, Y.; Cervantes-Salguero, K.; Minami, K.; Kawamata, I.; Nakanishi, W.; Hill, J. P.; Murata, S.; Ariga, K., Supramolecular 1-D Polymerization of DNA Origami through a Dynamic Process at the 2-Dimensionally Confined Air-Water Interface. *Phys. Chem. Chem. Phys.* **2016,** *18*, 12576-12581.

(69) Pinheiro, A. V.; Han, D.; Shih, W. M.; Yan, H., Challenges and Opportunities for Structural DNA Nanotechnology. *Nat. Nanotechnol.* **2011,** *6*, 763-772.

(70) Iwaura, R.; Iizawa, T.; Minamikawa, H.; Ohnishi-Kameyama, M.; Shimizu, T., Diverse Morphologies of Self-Assemblies from Homoditopic 1,18-Nucleotide-Appended Bolaamphiphiles: Effects of Nucleobases and Complementary Oligonucleotides. *Small* **2010,** *6*, 1131-1139.

(71) Nakamura, M.; Okaue, T.; Takada, T.; Yamana, K., DNA-Templated Assembly of Naphthalenediimide Arrays. *Chem. Eur. J.* **2012,** *18*, 196-201.

(72) Iwaura, R.; Ohnishi-Kameyama, M.; Iizawa, T., Construction of Helical J-Aggregates Self-Assembled from a Thymidylic Acid Appended Anthracene Dye and DNA as a Template. *Chem. Eur. J.* **2009,** *15*, 3729-3735.

(73) Puppels, G. J.; Otto, C.; Greve, J.; Robert-Nicoud, M.; Arndt-Jovin, D. J.; Jovin, T. M., Raman Microspectroscopic Study of Low-Ph-Induced Changes in DNA Structure of Polytene Chromosomes. *Biochemistry* **1994,** *33*, 3386-3395.

(74) Senanayak, S. P.; Ashar, A. Z.; Kanimozhi, C.; Patil, S.; Narayan, K. S., Room-Temperature Bandlike Transport and Hall Effect in a High-Mobility Ambipolar Polymer. *Phys. Rev. B* **2015,** *91*, 115302.

(75) Sirringhaus, H.; Brown, P. J.; Friend, R. H.; Nielsen, M. M.; Bechgaard, K.; Langeveld-Voss, B. M. W.; Spiering, A. J. H.; Janssen, R. A. J.; Meijer, E. W.; Herwig, P.; de Leeuw, D. M., Two-Dimensional Charge Transport in Self-Organized, High-Mobility Conjugated Polymers. *Nature* **1999,** *401*, 685-688.

(76) Oh, B. N.; Park, S.; Ren, J.; Jang, Y. J.; Kim, S. K.; Kim, J., Label-Free Emission Assay of Mercuric Ions Using DNA Duplexes of Poly(Dt). *Dalton Trans.* **2011,** *40*, 6494-6499.
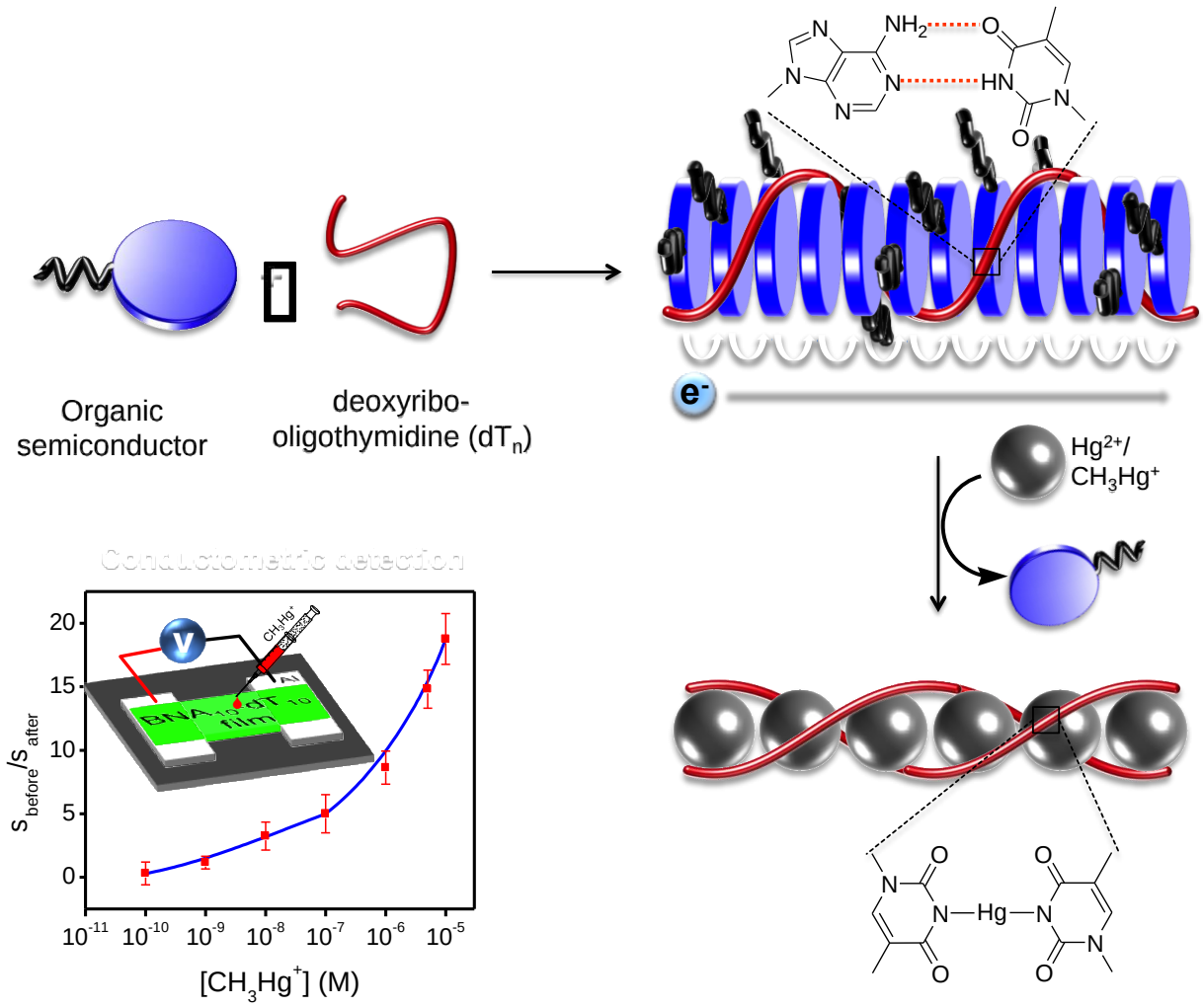
Table of Contents Graphic (only for TOC)